Remote sensing of penetrable objects buried beneath two-dimensional random rough surfaces by use of the Mueller matrix elements

Magda El-Shenawee

Department of Electrical Engineering, University of Arkansas, Fayetteville, Arkansas 72701

Received April 20, 2002; revised manuscript received July 30, 2002; accepted August 12, 2002

The modified Mueller matrix elements for electromagnetic scattering from penetrable objects buried under two-dimensional random rough surfaces are investigated. This matrix relates the incident to the scattered waves, and it contains different combinations of the fully polarimetric scattering matrix elements. The statistical average of each Mueller matrix element is computed on the basis of the Monte Carlo simulations by exploiting the speed of the three-dimensional steepest-descent fast multipole method. The numerical results clearly show that relying only on the co-polarized or the cross-polarized intensities or both (i.e., vv, hh, vh, and hv) is not sufficient for sensing the buried objects. However, examining all 16 Mueller matrix elements significantly increases the possibility of detecting these objects. This technique can be used in remote sensing of scatterers buried beneath the rough ground.

OCIS codes: 290.0290, 280.0280.

1. INTRODUCTION

Remote sensing of objects buried under the rough ground has tremendous civil and defense applications, e.g., archaeology discovery, mine detection, and sensing underground resources. In previous papers[1–3] the scattered electric near field was calculated to simulate ground-penetrating radar measurements. A single penetrable or perfect electric conductor object or both was buried under the rough ground; the average of the scattered electric near fields over the azimuth angle was presented in Ref. 1, and the average over the rough surface realizations was presented in Ref. 2. In Ref. 3 two dielectric objects were buried under the random rough ground, and the electromagnetic near-field interference between the objects was studied. The reported results showed the significant distortion in the near-field signals caused by the presence of the rough air–ground interface. In Refs. 1–3 the signature of the target was often obtained by removing the background from the received signals (i.e., by subtracting the scattering from the rough ground with no buried objects). In Ref. 4 the angular correlation function and the radar cross section (RCS) were presented for a perfect electric conductor sphere buried under the rough ground, and the authors presented the advantage of computing the angular correlation function over the RCS. In Ref. 5 the 16 Mueller matrix elements were analytically obtained for scattering from a coated two-dimensional random rough surface in which the configuration represented a three-layer geometry (the air and two layers of rough interfaces) with no buried objects. The Mueller matrix elements, which relate the incident to the scattered waves, are defined in terms of the modified Stokes vector.[6–8] The results reported in Ref. 5 showed a great sensitivity of some Mueller matrix elements (m_{34} and m_{43}) in the backscatter direction to the thickness of the coated layer. In other words, these two elements showed considerable differences owing to the underground inhomogeneity, which was not the case for the other Mueller matrix elements (m_{11}, m_{12}, m_{22}, etc.). This finding is the motivation of the current paper; however, the configuration here represents two different dielectric objects buried under the two-dimensional random rough ground as shown in Fig. 1 below.

It is necessary to differentiate between the results reported in Ref. 2 and the current paper. In Ref. 2 the statistical average of the buried object's signature was computed on the basis of the scattered electric fields in the near zone. In the current paper, the statistical average of the scattered electric fields from one or two or both buried objects is calculated in the far zone and presented in terms of the Mueller matrix elements. More important, the subtraction process often used in Refs. 1–3 is not used in the current paper. In other words, the far fields scattered from the rough ground with the buried objects are directly compared with those scattered from the rough ground with no buried objects.

The formulations of the problem are given in Section 2, the numerical results are presented in Section 3, and the conclusions are stated in Section 4. More details are given in Appendixes A and B.

2. FORMULATIONS

The integral equation-based rigorous electromagnetic model was developed in Ref. 3 for scattering from multiple objects buried under the rough ground. This technique is employed to calculate the unknown method-of-moments surface currents on the rough ground and on both buried objects (see Fig. 1). The inhomogeneous scatterer is composed of four different regions: the air,

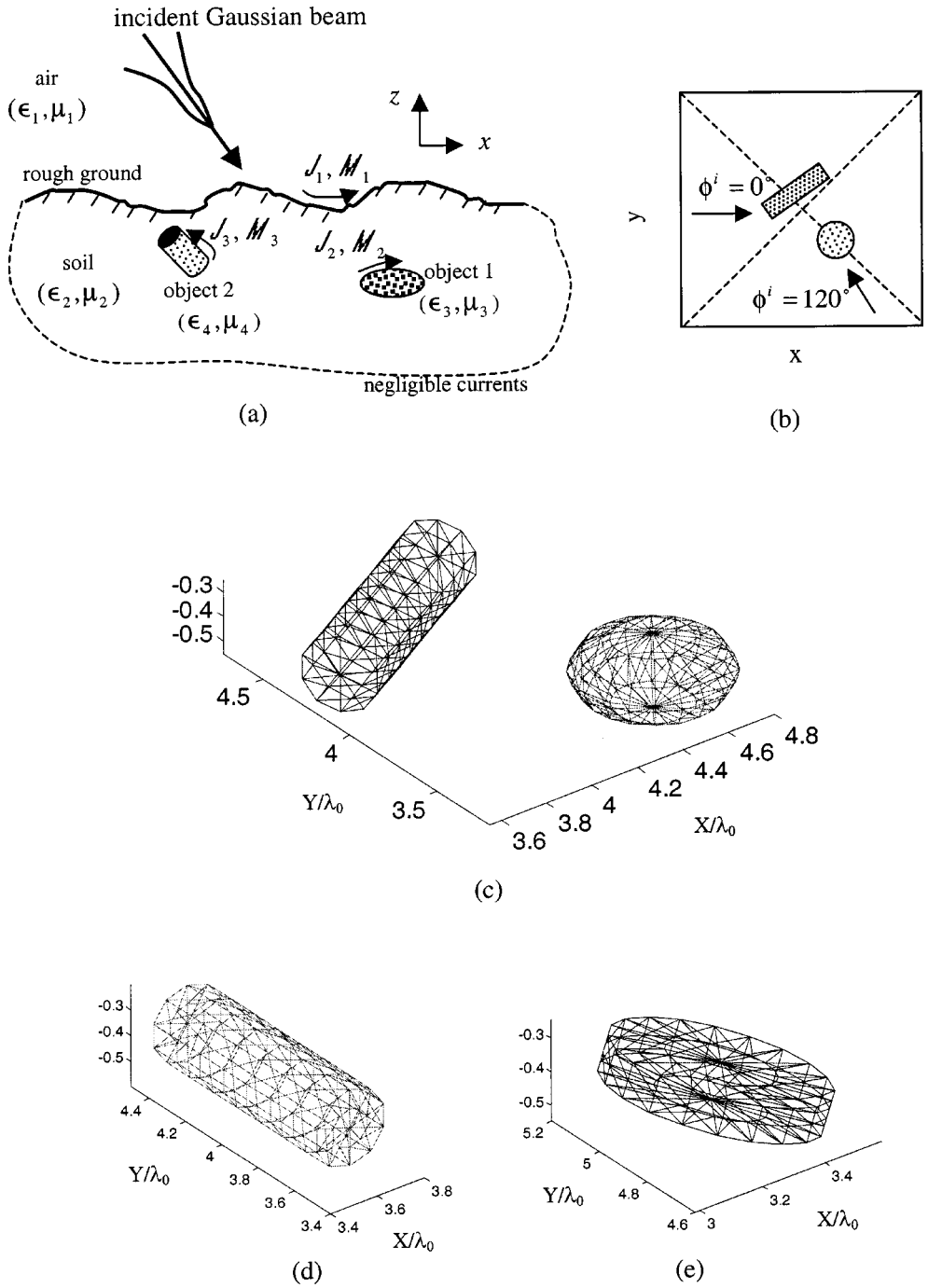

Fig. 1. (a) Cross section of a general two-dimensional rough ground with two buried objects. (b) Top view of the geometry. (c) Three-dimensional geometry for the buried spheroid and the 30°-tilted horizontal cylinder. (d) Three-dimensional geometry for the buried 90°-tilted horizontal cylinder. (e) Three-dimensional geometry for the buried 20°-tilted disk. All figures in (c)–(e) show exact locations of the objects.

the ground, and two different materials for the objects, where the relative permittivity and permeability are ϵ_1 and μ_1 for the air, ϵ_2 and μ_2 for the ground, ϵ_3 and μ_3 for the first object, and ϵ_4 and μ_4 for the second object. The unknown equivalent electric and magnetic surface currents are $\mathbf{J}_1$ and $\mathbf{M}_1$ on the ground, $\mathbf{J}_2$ and $\mathbf{M}_2$ on the first object, and $\mathbf{J}_3$ and $\mathbf{M}_3$ on the second object. The final set of surface-integral equations for the ground (S_1), The first object (S_2), and the second object (S_3) are given by[1,3,9]

$$\mathbf{E}^{\text{inc}}(\mathbf{r})|_{\text{tang}} = [(L_1 + L_2)\mathbf{J}_1 - (K_1 + K_2)\mathbf{M}_1 - L_3\mathbf{J}_2 + K_3\mathbf{M}_2 - L_4\mathbf{J}_3 + K_4\mathbf{M}_3]_{\text{tang}}, \quad \mathbf{r} \in S_1, \tag{1a}$$

$$\mathbf{H}^{\mathrm{inc}}(\mathbf{r})|_{\mathrm{tang}} = \Bigg[(K_1 + K_2)\mathbf{J}_1 + \left(\frac{L_1}{\eta_1^2} + \frac{L_2}{\eta_2^2}\right)\mathbf{M}_1 - K_3\mathbf{J}_2 - \frac{L_3}{\eta_2^2}\mathbf{M}_2 - K_4\mathbf{J}_3 - \frac{L_4}{\eta_2^2}\mathbf{M}_3\Bigg]_{\mathrm{tang}}, \quad \mathbf{r} \in S_1, \tag{1b}$$

$$0 = [-L_2\mathbf{J}_1 + K_2\mathbf{M}_1 + (L_3 + L_5)\mathbf{J}_2 - (K_3 + K_5)\mathbf{M}_2 + L_4\mathbf{J}_3 - K_4\mathbf{M}_3]_{\mathrm{tang}}, \quad \mathbf{r} \in S_2, \tag{1c}$$

$$0 = \Bigg[-K_2\mathbf{J}_1 - \frac{L_2}{\eta_2^2}\mathbf{M}_1 + (K_3 + K_5)\mathbf{J}_2 + \left(\frac{L_3}{\eta_2^2} + \frac{L_5}{\eta_3^2}\right)\mathbf{M}_2 + K_4\mathbf{J}_3 + \frac{L_4}{\eta_2^2}\mathbf{M}_3\Bigg]_{\mathrm{tang}}, \quad \mathbf{r} \in S_2, \tag{1d}$$

$$0 = [-L_2\mathbf{J}_1 + K_2\mathbf{M}_1 + L_3\mathbf{J}_2 - K_3\mathbf{M}_2 + (L_4 + L_6)\mathbf{J}_3 - (K_4 + K_6)\mathbf{M}_3]_{\mathrm{tang}}, \quad \mathbf{r} \in S_3, \tag{1e}$$

$$0 = \Bigg[-K_2\mathbf{J}_1 + \frac{L_2}{\eta_2^2}\mathbf{M}_1 + K_3\mathbf{J}_2 + \frac{L_3}{\eta_2^2}\mathbf{M}_2 + (K_4 + K_6)\mathbf{J}_3 + \left(\frac{L_4}{\eta_2^2 2} + \frac{L_6}{\eta_4^2}\right)\mathbf{M}_3\Bigg]_{\mathrm{tang}}, \quad \mathbf{r} \in S_3, \tag{1f}$$

in which the intrinsic impedance in $\eta_i = \sqrt{\mu_i/\epsilon_i}$, with $i = 1, 2, \ldots 4$, and L_j and K_j, $j = 1, 2, \ldots 6$, are the integrodifferential operators as summarized in Appendix A.[1,3,9] The surfaces of the rough ground and the two objects are discretized into triangular patches in which the unknown equivalent electric and magnetic currents in Eqs. (1) are approximated by use of the Rao–Wilton–Glisson vector basis functions $\mathbf{j}(\mathbf{r})$[9,10] as

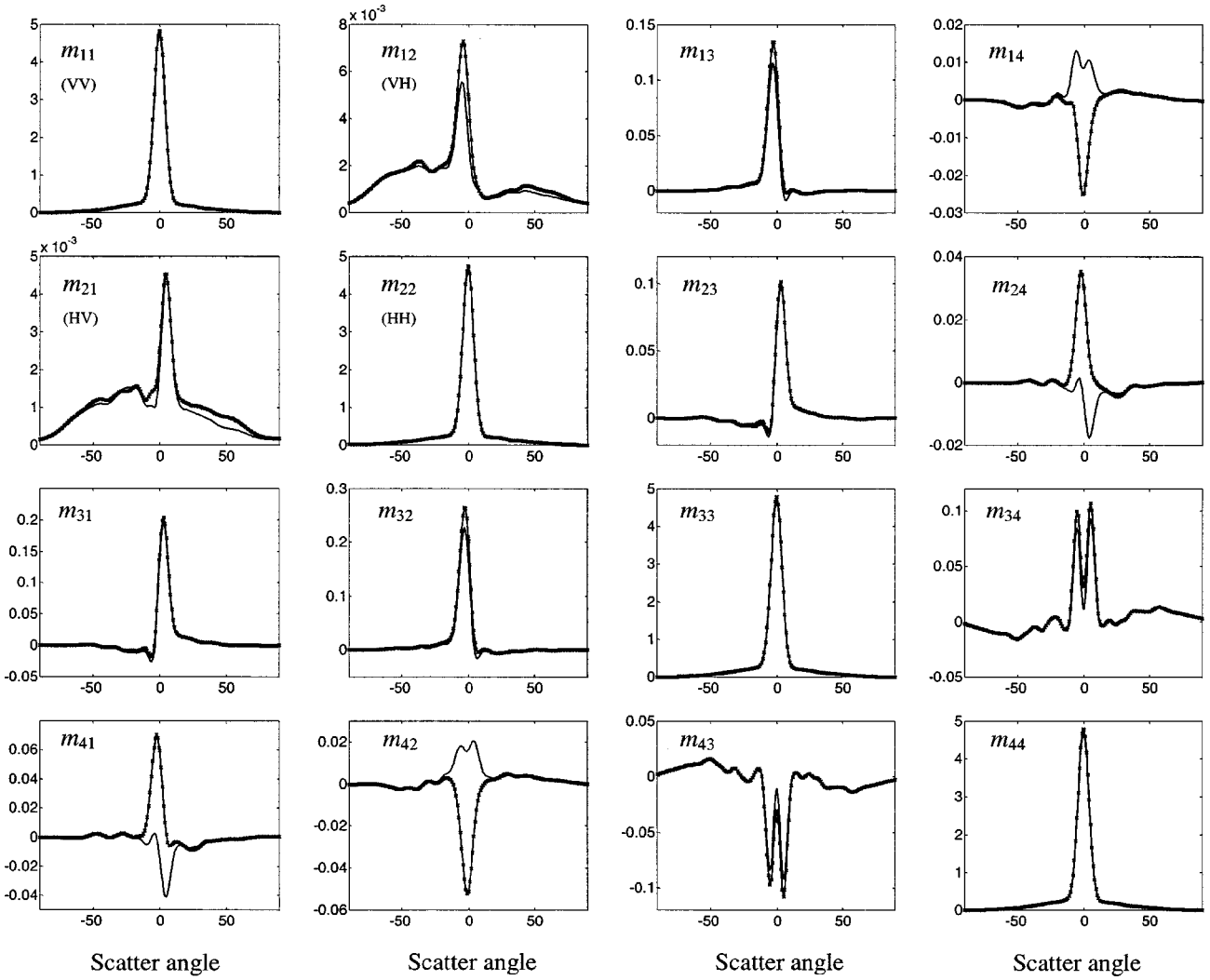

Fig. 2. Normalized bistatic modified Mueller matrix elements (total intensity): $m_{11}, m_{12}, \ldots, m_{44}$. Solid curve, for the rough ground only; cross symbol, for the rough ground with the two buried objects [the spheroid and the horizontal 30°-tilted cylinder, Fig. 1(c)] for incident angles $\theta^i = 0°$ and $\phi^i = 0°$. Monte Carlo for 100 rough surface realizations.

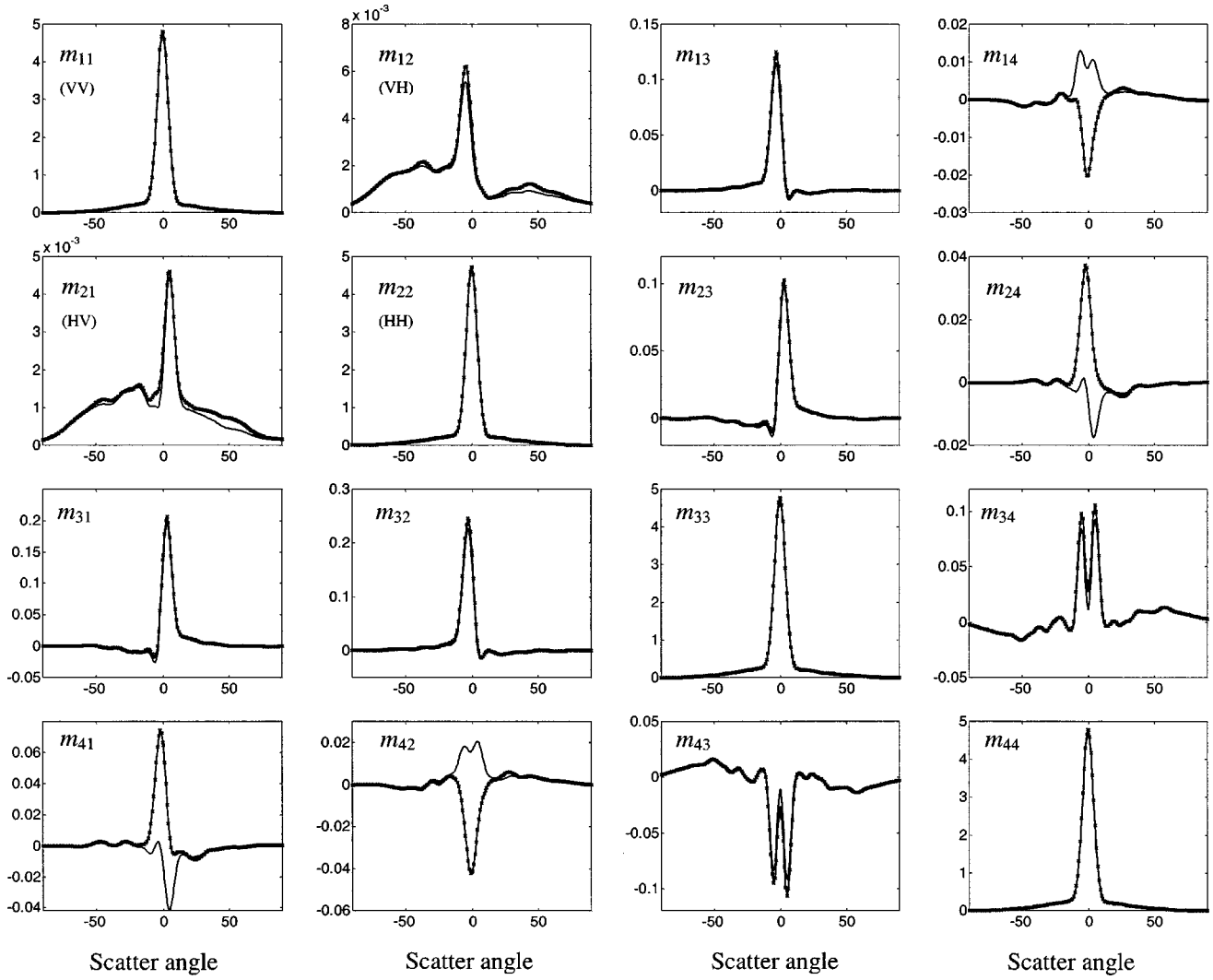

Fig. 3. Normalized bistatic modified Mueller matrix elements (total intensity): $m_{11}, m_{12}, \ldots, m_{44}$. Solid curve, for the rough ground only; cross symbol, for the rough ground with only the second object [horizontal 30°-tilted cylinder, Fig. 1(c)] for the incident angles $\theta^i = 0°$ and $\phi^i = 0°$. Monte Carlo for 100 rough surface realizations.

$$\mathbf{J}_k(\mathbf{r}) = \sum_{n=1}^{N_k} I_n^{(k)} \mathbf{j}_n^{(k)}(\mathbf{r}), \qquad \mathbf{M}_k(\mathbf{r}) = \eta_1 \sum_{n=1}^{N_k} I_{(n+N_k)}^{(k)} \mathbf{j}_n^{(k)}(\mathbf{r}),$$

$$\mathbf{r} \in S_k, \quad \text{for } k = 1, 2, 3. \tag{2}$$

After some algebraic manipulations, the linear system of equations is obtained as $\mathcal{Z}\mathcal{I} = \mathcal{V}$ (as summarized in Appendix B), where the total impedance matrix $\mathcal{Z}$ has order $2(N_1 + N_2 + N_3) \times 2(N_1 + N_2 + N_3)$. The number of surface unknowns on the ground, the first object, and the second object are $2N_1$, $2N_2$, and $2N_3$, respectively. The vector $\mathcal{V}$ represents the tested tangential incident electric field $\mathbf{E}^{\text{inc}}$ and normalized magnetic field $\eta_1 \mathbf{H}^{\text{inc}}$ on the exterior surface of the ground. The steepest-descent fast multipole method[11] (SDFMM) was implemented in Refs. 1–3 to dramatically accelerate solving for the unknown surface-current coefficients $\mathcal{I}$. Once the unknown surface currents are obtained, the scattered electric fields in the far zone can be computed.[12]

For the modified Mueller matrix elements,[5–8] we are following the notation used in Ref. 7 in which the normalized modified Stokes vector is given by

$$I = \begin{pmatrix} |E_v|^2 \\ |E_h|^2 \\ 2\,\mathrm{Re}(E_v E_h^*) \\ 2\,\mathrm{Im}(E_v E_h^*) \end{pmatrix} \Big/ \eta_1, \tag{3a}$$

in which v and h represent the vertical and horizontal polarizations, respectively; thus from Ref. 7

$$I^s = \frac{1}{r^2} M_m I^i, \tag{3b}$$

where the superscripts s and i represent the scattered and incident waves, respectively. The modified Mueller matrix M_m is given by[7]

$$M_m = \begin{bmatrix} |S_{vv}|^2 & |S_{vh}|^2 & \mathrm{Re}(S_{vh}^* S_{vv}) & -\mathrm{Im}(S_{vh}^* S_{vv}) \\ |S_{hv}|^2 & |S_{hh}|^2 & \mathrm{Re}(S_{hv} S_{hh}^*) & -\mathrm{Im}(S_{hv} S_{hh}^*) \\ 2\,\mathrm{Re}(S_{vv} S_{hv}^*) & 2\,\mathrm{Re}(S_{vh} S_{hh}^*) & \mathrm{Re}(S_{vv} S_{hh}^* + S_{vh} S_{hv}^*) & -\mathrm{Im}(S_{vv} S_{hh}^* - S_{vh} S_{hv}^*) \\ 2\,\mathrm{Im}(S_{vv} S_{hv}^*) & 2\,\mathrm{Im}(S_{vh} S_{hh}^*) & \mathrm{Im}(S_{vv} S_{hh}^* + S_{vh} S_{hv}^*) & \mathrm{Re}(S_{vv} S_{hh}^* - S_{vh} S_{hv}^*) \end{bmatrix}, \quad (3c)$$

where S_{pq} is the p-polarized scattered waves that are due to the q-polarized incident waves ($p, q = v, h$) as described in the fully polarimetric scattering matrix S[7]:

$$\begin{pmatrix} E_v^s \\ E_h^s \end{pmatrix} = \frac{\exp(jkr)}{r} \begin{bmatrix} S_{vv} & S_{vh} \\ S_{hv} & S_{hh} \end{bmatrix} \begin{pmatrix} E_v^i \\ E_h^i \end{pmatrix}, \quad (3d)$$

where $E_{v,h}^i$ and $E_{v,h}^s$ are the vertically and horizontally polarized incident and scattered electric fields in the far zone, respectively.

3. NUMERICAL RESULTS AND DISCUSSIONS

The random rough surface characterized with Gaussian statistics for simulating the ground is generated 100 times for the configuration shown in Fig. 1. The linear system of equations is solved for each random surface realization for both the vertically and the horizontally polarized incident waves. Each set of the Monte Carlo simulations to obtain the average scattered intensity is based on the 100 independent realizations. The 16 modified Mueller matrix elements in Eq. (3c) are calculated for the total scattered waves (i.e., not for the incoherent scattered waves). By use of the standard matrix notations in Eq. (3c), these elements are $m_{11} = \langle |S_{vv}|^2 \rangle$, $m_{22} = \langle |S_{hh}|^2 \rangle$, $m_{14} = -\mathrm{Im}(\langle S_{vh}^* S_{vv} \rangle)$, etc., where the angle brackets denote the ensemble average. All Mueller matrix elements presented here are normalized by the factor $4\pi/(2\eta_0 A_z P^i)$, where A_z, η_0, and P^i are the footprint

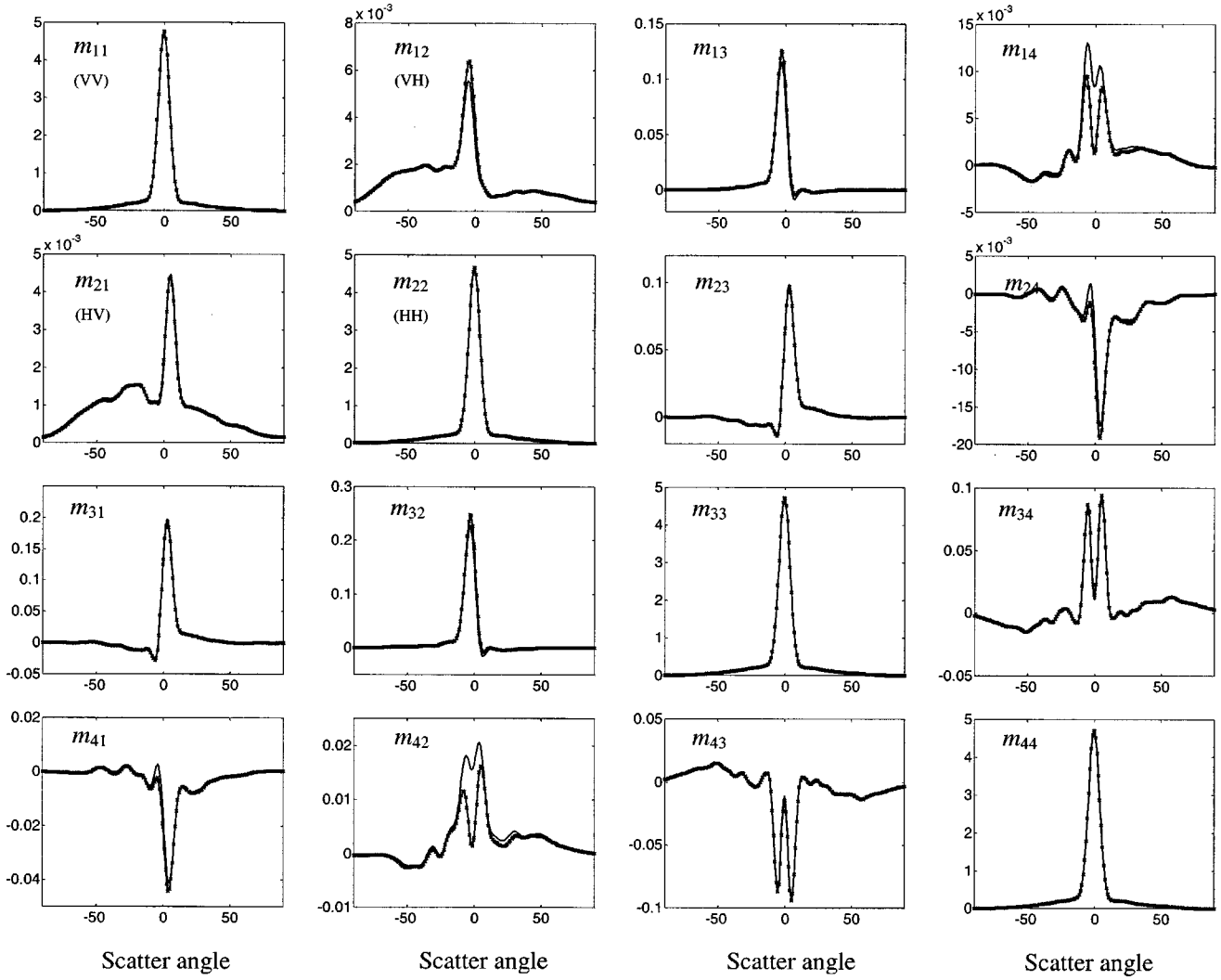

Fig. 4. Normalized bistatic modified Mueller matrix elements (total intensity): $m_{11}, m_{12}, \ldots, m_{44}$. Solid curve, for the rough ground only; the cross symbol, for the rough ground with only the first object [the spheroid, Fig. 1(c)] for the incident angles $\theta^i = 0°$ and $\phi^i = 0°$. Monte Carlo for 100 rough surface realizations.

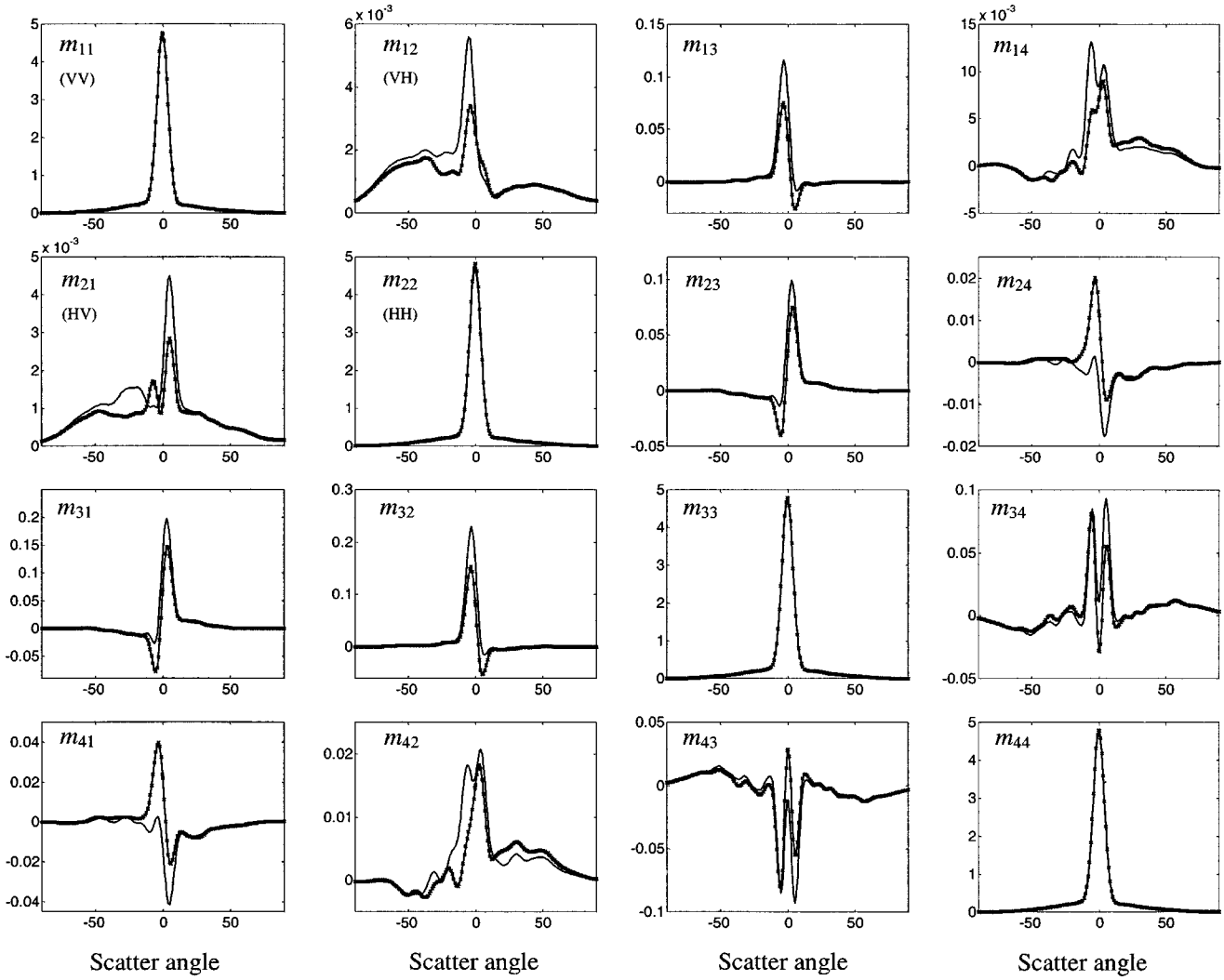

Fig. 5. Normalized bistatic modified Mueller matrix elements (total intensity): $m_{11}, m_{12}, \ldots, m_{44}$. Solid curve, for the rough ground only; cross symbol, for the rough ground with only the second object [horizontal 90°-tilted cylinder, Fig. 1(d)] for the incident angles $\theta^i = 0°$ and $\phi^i = 0°$. Monte Carlo for 100 rough surface realizations.

area on the ground, the intrinsic impedance of the free space, and the total incident power. With this normalization, the element m_{11} becomes the normalized vertically copolarized RCS (vv), the element m_{22} becomes the normalized horizontally copolarized RCS (hh), the element m_{12} becomes the normalized cross-polarized RCS (vh), and the element m_{21} is the normalized cross-polarized RCS (hv). For the incident tapered Gaussian beam used in this paper,[5,13] the total incident power is the sum of the power in each plane wave.[14] Similar to the previous work[1–3] the dimensions of the ground are assumed to be $8\lambda_0 \times 8\lambda_0$ with Gaussian half-beam width equal to $1.6\lambda_0$ centered on the ground at $4\lambda_0$, $4\lambda_0$, where λ_0 is the free-space wavelength.

In this paper the first object is modeled as an oblate spheroid ($a = 0.15\lambda_0$, $b = 0.3\lambda_0$), and the second object is modeled as a circular cylinder ($a = 0.15\lambda_0$, $h = 0.9\lambda_0$) or a circular disk ($a = 0.3\lambda_0$, $h = 0.1\lambda_0$) as shown in Figs. 1(c)–1(e). The locations of these objects vary in each example. The rms height and the correlation length of the rough ground are assumed to be $\sigma = 0.1\lambda_0$ and $l_c = 0.5\lambda_0$, respectively. The relative dielectric constants of the ground, the cylinder, the spheroid, and the disk are assumed as $\epsilon_r = 2.5 - j0.18$, $\epsilon_r = 4.0$, $\epsilon_r = 2.9 - j0.072$, and $\epsilon_r = 4.0$, respectively. The total number of surface-current unknowns is 61,200 for the geometry shown in Fig. 1, where $2N_1 = 60{,}000$ (on the ground surface), $2N_2 = 600$ (on the first object), and $2N_3 = 600$ (on the second object).[3] These numbers of unknowns are the result of discretizing the ground surface into 10,101 nodes and 20,000 triangular patches and discretizing each object into 102 nodes and 200 triangular patches, and they are kept the same for all the cases discussed in this section.

In example 1 a spheroid and a horizontal cylinder are buried under the ground. The spheroid's center is located at $x = 4.5\lambda_0$, $y = 3.5\lambda_0$, and $z = -0.4\lambda_0$, and the horizontal cylinder is tilted by 30° with the x axis and is located at $x = 4.01\lambda_0$, $y = 4.375\lambda_0$, and $z = -0.4\lambda_0$ measured from the axis midpoint [see Fig. 1(c)]. For $\theta^i = 0°$, $\phi^i = 0°$, the ensemble average for each modified Mueller matrix element is plotted versus the scatter angle as presented in Fig. 2. As expected, the results show that all the diagonal elements of the Mueller matrix

have maximum values approximately in the specular direction ($\theta^i = 0°$). Interestingly, the elements m_{14}, m_{24}, m_{41}, and m_{42} show a distinguished signature for the rough ground with the two buried objects that is different from the rough ground alone (i.e., with no buried objects). Moreover, the elements m_{12}, m_{21}, m_{32}, m_{13}, m_{34}, and m_{43} show slight differences between these two cases. However, the diagonal elements m_{11}, m_{22}, m_{33}, and m_{44} show almost no differences between the two cases.

It is important to investigate whether the significant differences shown in Fig. 2 are due to the interference between the objects or due to other causes. Therefore additional results for the cylinder and the spheroid, when each is buried alone under the same rough ground, are presented in Figs. 3 and 4, respectively. Each object is buried in its original location under the random rough ground as discussed in the data of Fig. 2. The results in Fig. 3 show the same observations as in Fig. 2; i.e., the elements m_{14}, m_{24}, m_{41}, and m_{42} clearly show an indication to the presence of the cylinder under the ground, whereas the elements m_{11} and m_{22} show no such indication.

The results in Fig. 4, for the buried spheroid alone, show that only elements m_{42} and m_{14} indicate the presence of the spheroid. In other words, the results in Figs. 3 and 4 clearly show the significant sensitivity of some of the Mueller matrix elements to the presence of buried objects. The sensitivity level of these elements clearly depends on the object's orientation, material, and size as presented in Figs. 2–4. It is interesting to note that the expressions of m_{14}, m_{24}, m_{41}, and m_{42} as given in Eq. (3c) are the imaginary parts of the product of the co- and cross-polarized scattering elements. This implies that these elements contain some phase information, which is not the case for the other elements, e.g., m_{11} and m_{22}. The results in Figs. 2–4 clearly indicate that if one relies only on the co- or the cross-polarized intensities (i.e., m_{11}, m_{22}, m_{12}, and m_{21}) or both it might not be possible to detect the buried objects. However, investigating all 16 Mueller matrix elements significantly increases the possibility of detecting these objects.

In example 2 the cylinder's orientation effect is investigated while keeping in mind the rest of the data of Fig. 2. Therefore the cylinder is tilted 90° to the x axis and is

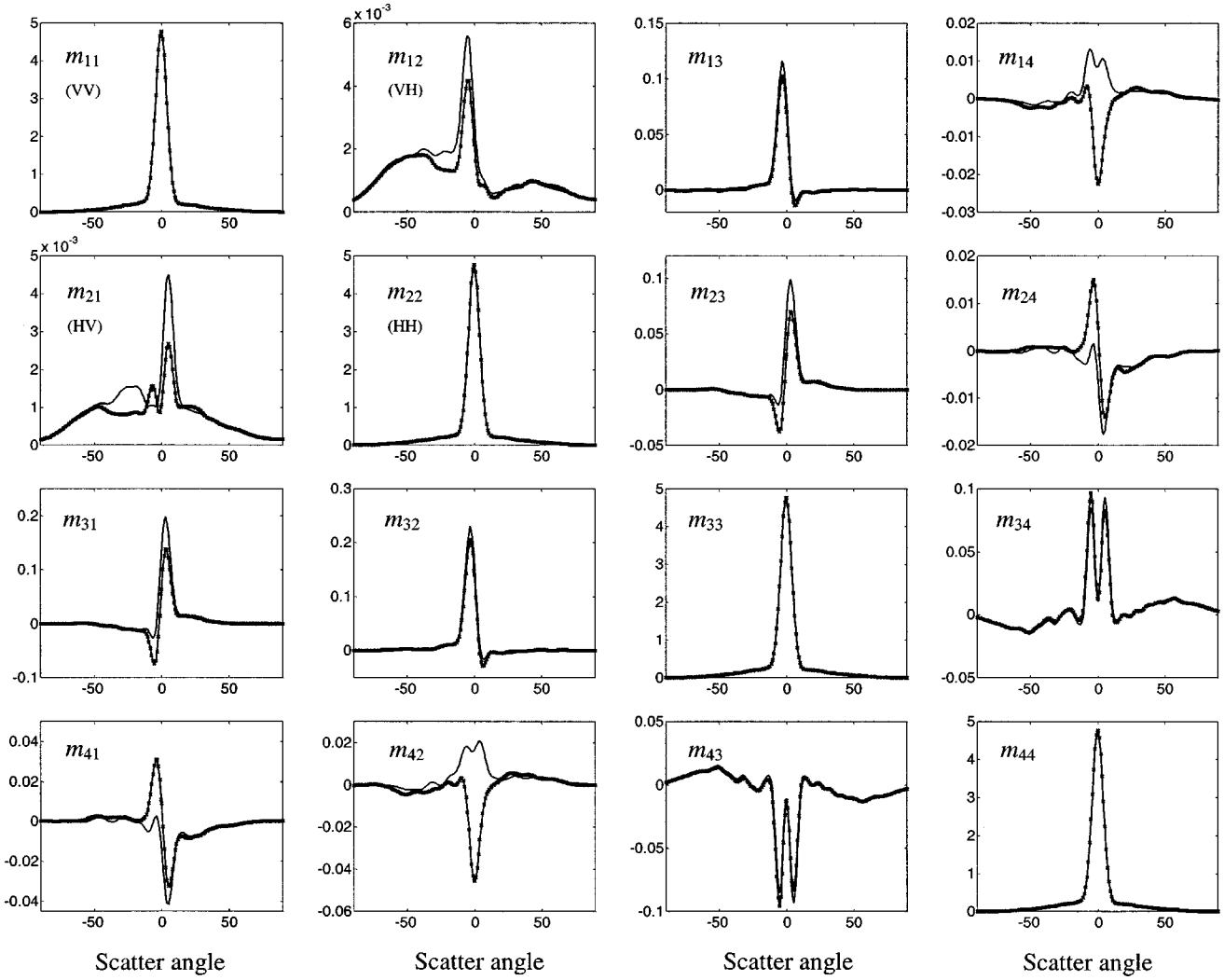

Fig. 6. Normalized bistatic modified Mueller matrix elements (total intensity): $m_{11}, m_{12}, \ldots, m_{44}$. Solid curve, for the rough ground only; cross symbol, for the rough ground with only the second object [20°-tilted disk, Fig. 1(e)] for the incident angles $\theta^i = 0°$ and $\phi^i = 0°$. Monte Carlo for 100 rough surface realizations.

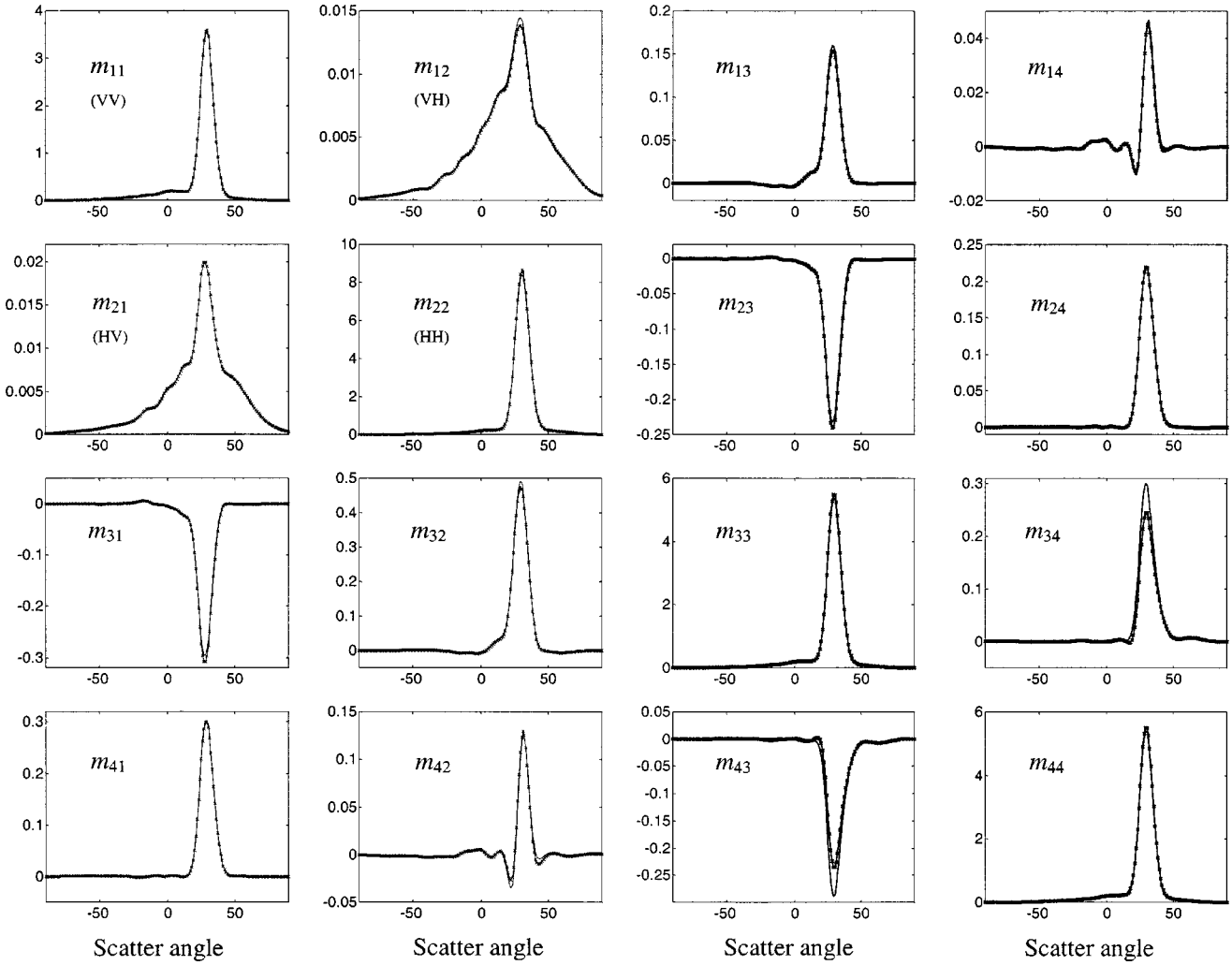

Fig. 7. Normalized bistatic modified Mueller matrix elements (total intensity): $m_{11}, m_{12}, \ldots, m_{44}$. Solid curve, for the rough ground only; cross symbol, for the rough ground with the two buried objects [the spheroid and the horizontal 30°-tilted cylinder, Fig. 1(c)] for the incident angles $\theta^i = 30°$ and $\phi^i = 120°$. Monte Carlo for 100 rough surface realizations.

buried alone under the rough interface. The midpoint of the axis is located at $x = 3.6\lambda_0$, $y = 4.0\lambda_0$, and $z = -0.4\lambda_0$ [see Fig. 1(d)]. As shown in Fig. 5, almost 12 of the 16 elements show considerable differences owing to the presence of the cylinder. A comparison of the results of Figs. 3 and 5, in which the same size and material of the horizontal cylinder are used, shows that the cylinder's orientation plays an effective role in the sensitivity level of these elements. The depolarization level of the scattered waves from the rough ground with the buried cylinder varies with the orientation of the cylinder, leading to observed variation in some of the Mueller matrix elements.

In example 3 the cylinder is replaced with a circular disk tilted by 20° with the z axis and made of the same material (i.e., $\epsilon_r = 4.0$). The center of its top circle is located at $x = 3.3\lambda_0$, $y = 4.9\lambda_0$, $z = -0.35\lambda_0$ and is buried alone under the rough ground [see Fig. 1(e)]. Again, the results plotted in Fig. 6 show that some of the Mueller matrix elements indicate the presence of the disk. In particular, the elements m_{14}, m_{24}, m_{41}, m_{42}, m_{12}, and m_{21} show considerable differences between the rough ground only and the rough ground with the buried disk. Consistent with the previous examples, the vv or hh intensities (i.e., m_{11} and m_{22}) show almost no differences between the two cases.

In example 4 the Mueller elements for the spheroid and the horizontal cylinder, both buried under the ground (same data of Fig. 2), are computed at different incident angles, $\theta^i = 30°$, $\phi^i = 120°$, as shown in Fig. 7. None of the elements in the current case show any indication of the presence of the buried objects except for the elements m_{34} and m_{43}. In addition, all the elements in this case are significantly different from those presented in Fig. 2, which shows their dependency on the incident angles. In this example, the far fields are computed in the same plane of incidence, i.e., at $0° \leqslant \theta^s \leqslant 90°$ for $\phi^s = 120°$ and for $\phi^s = 300°$.

As mentioned earlier, in examples 1–4, all the Mueller matrix elements represent the average values based on the Monte Carlo simulations of 100 rough surface realizations. This indicates that the observed sensitivity of some of these elements is consistent for all rough surface realizations since it survived the averaging process. To investigate this point, as an example, we plot the elements m_{42}, m_{14}, and m_{24} for the scattered waves from

only one rough surface realization as shown in Fig. 8. The numerical results show that these elements for the rough ground alone are different from all the other buried scatterers. This observation indicates that investigating all the Mueller matrix elements can be very useful in detecting the buried objects under the realistic rough ground represented here by one rough surface realization.

The above results support the observation reported in Ref. 5 in which the underground inhomogeneity was caused by the presence of the coated irregular layer above the rough ground, whereas here the inhomogeneity is due to the presence of dielectric objects buried beneath the ground. As mentioned in Ref. 7, the modified Mueller matrix, in general, is not symmetric, which is demonstrated in all figures. However, in all results it is observed that $m_{34} \approx -m_{43}$, which can be attributed to the slight cross polarization caused by the small roughness parameters considered in this paper. For the same reason, it is observed that $m_{33} \approx m_{44}$ in all figures. However, in Figs. 2–6 it is observed, as expected, that $m_{11} \approx m_{22}$ (normal incidence case), whereas in Fig. 7 $m_{22} > m_{11}$ (oblique incidence case). In Fig. 7 the incident electric field for the h polarization is parallel to the axis of the buried cylinder, whereas for the v polarization, it is perpendicular to cylinder axis [see Fig. 1(b)].

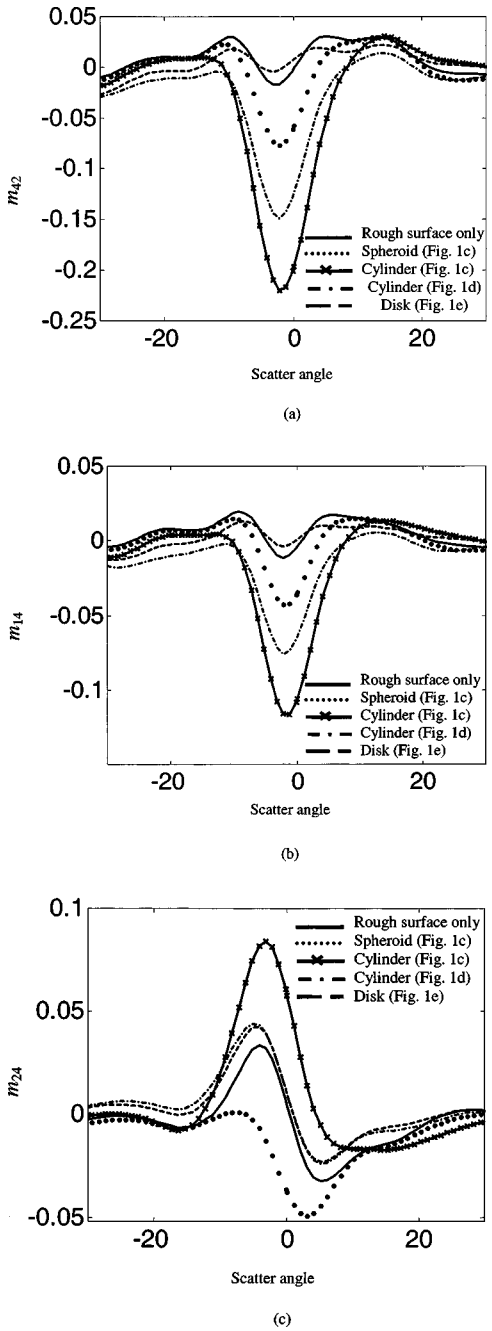

Fig. 8. Normalized bistatic modified Mueller matrix (a) element m_{42}, (b) element m_{14}, and (c) m_{24} versus the scatter angle for $\theta^i = 0°$ and $\phi^i = 0°$ from the only one rough surface realization. No averaging.

Note that element $m_{12} \neq$ element m_{21} because all the Mueller matrix elements presented here are for the bistatic case and not for the backscatter case. Even though it is more practical for remote-sensing applications to consider the backscatter case, the bistatic results showed the considerable sensitivity of some Mueller matrix elements to the presence of buried objects. In addition, calculating the average of these elements in the backscatter direction will be computationally more expensive.

Examining the Mueller matrix expression in Eq. (3c), it is clear that several elements are functions of the amount of wave depolarization. This could be one of the reasons that the Mueller elements for the tilted cylinder are the most distinguished ones as shown in the numerical results. The materials, locations of the buried scatterers, and their contrast with the surrounding underground medium have impact on these elements as well. More work need to be conducted to investigate how the ground roughness affects these elements since in this paper we assumed small roughness parameters.

The sensitivity of Mueller matrix elements, with respect to the surface profile, is examined to emphasize the practical situation in which there is only one realization of the rough surface above the objects. Owing to the limited space, the elements m_{11} and m_{41} for the 30°-tilted cylinder case, shown in Fig. 1(c), are presented in Figs. 9(a) and 9(b), respectively. In these figures, the results from 20 individual rough surface profiles are plotted for rough surface alone and rough surface with the buried cylinder. These 20 profiles were selected out of the 100 used in the Monte Carlo simulations in steps of five, i.e., rough profile #1, #6, #11, . . . , and #96. The results in Fig. 9(a) show almost no difference between elements for the rough surface with or without the buried cylinder in all 20 individual profiles. However, the element m_{11} (vv) slightly varies from one profile to another [e.g., the maximum magnitude varies from 4.5 to 7, as shown in Fig. 9(a)]. In Fig. 9(b) the element m_{41} is presented for the same 20 individual rough surface profiles. In contrast, Fig. 9(b) shows distinct differences between elements for rough surface with and without the buried cylinder in all 20 profiles. Indeed, both the difference levels and the curve shapes greatly change from one profile to another, but all 20 results show that the element m_{41} can be used in sensing the buried cylinder in this case. A comparison of Fig. 9(a) with Fig. 9(b) shows that the element m_{41} is more sensitive to the surface profile than the element m_{11}. This can be explained by the sensitivity of the depolarized waves with the rough surface profile,

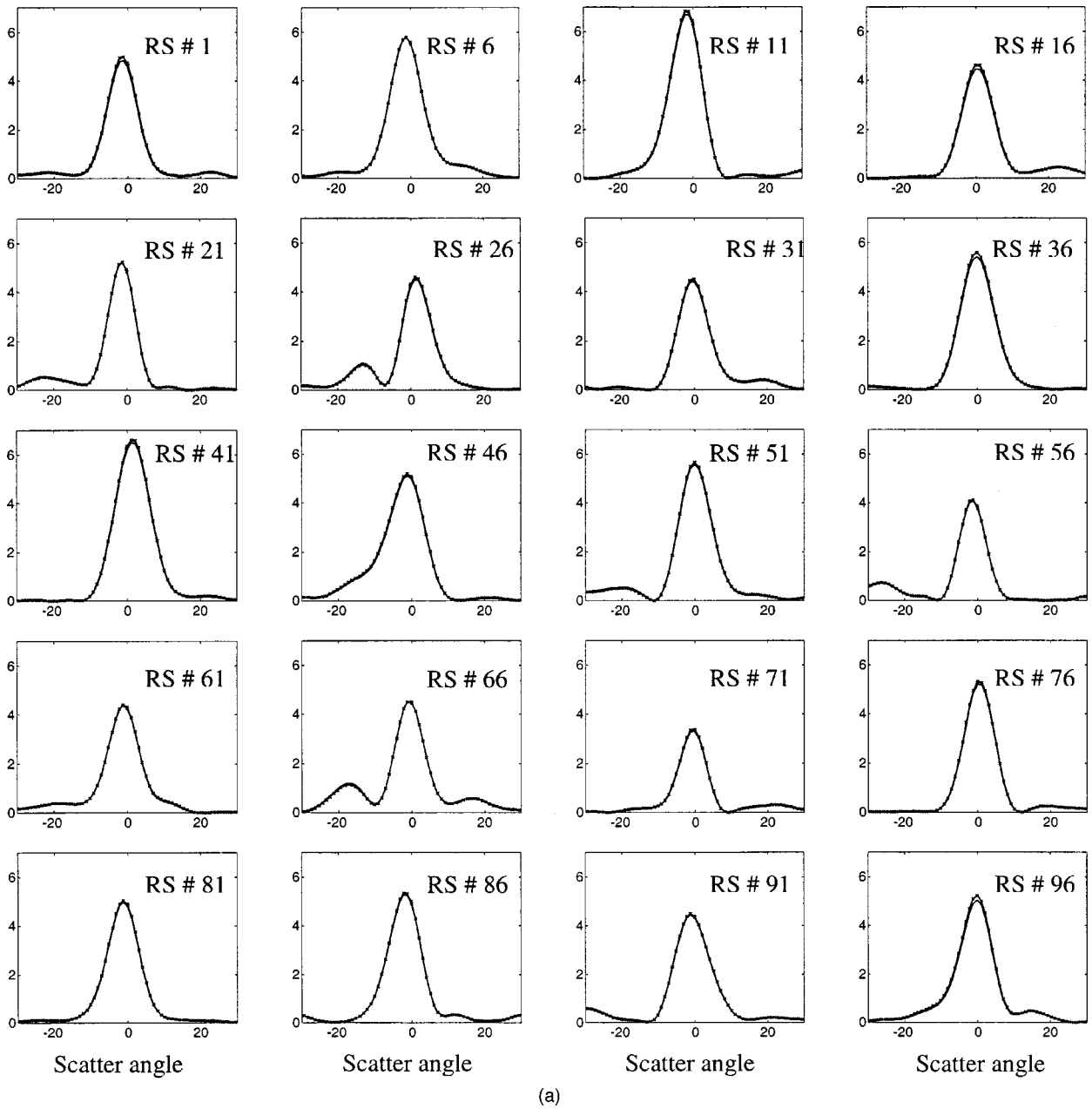

Fig. 9. Continues on next page.

which consequently affects some of the elements that are functions of depolarized waves, such as m_{41}, shown in Fig. 9(b).

4. CONCLUSIONS

The fast three-dimensional SDFMM computer code is used to calculate the average of each modified Mueller matrix element for the scattering from dielectric objects buried under the random rough ground. The statistical average for each element is computed by use of the Monte Carlo simulation. These simulations are obtained by running the three-dimensional SDFMM computer code hundreds of times, which shows the great advantage of using the fast multipole method. The numerical results clearly show that if one relies only on the co-polarized or the cross-polarized intensities or both it is very difficult to sense the buried objects. However, investigating all 16 Mueller matrix elements significantly help in detecting these objects.

APPENDIX A

With representation of the surface electric and magnetic currents $\mathbf{J}$ and $\mathbf{M}$ on S_1, S_2, and S_3 by the vector $\mathbf{X}$, the integrodifferential operators L_j and K_j, $j = 1, 2, \ldots 6$, are[1,3,9]

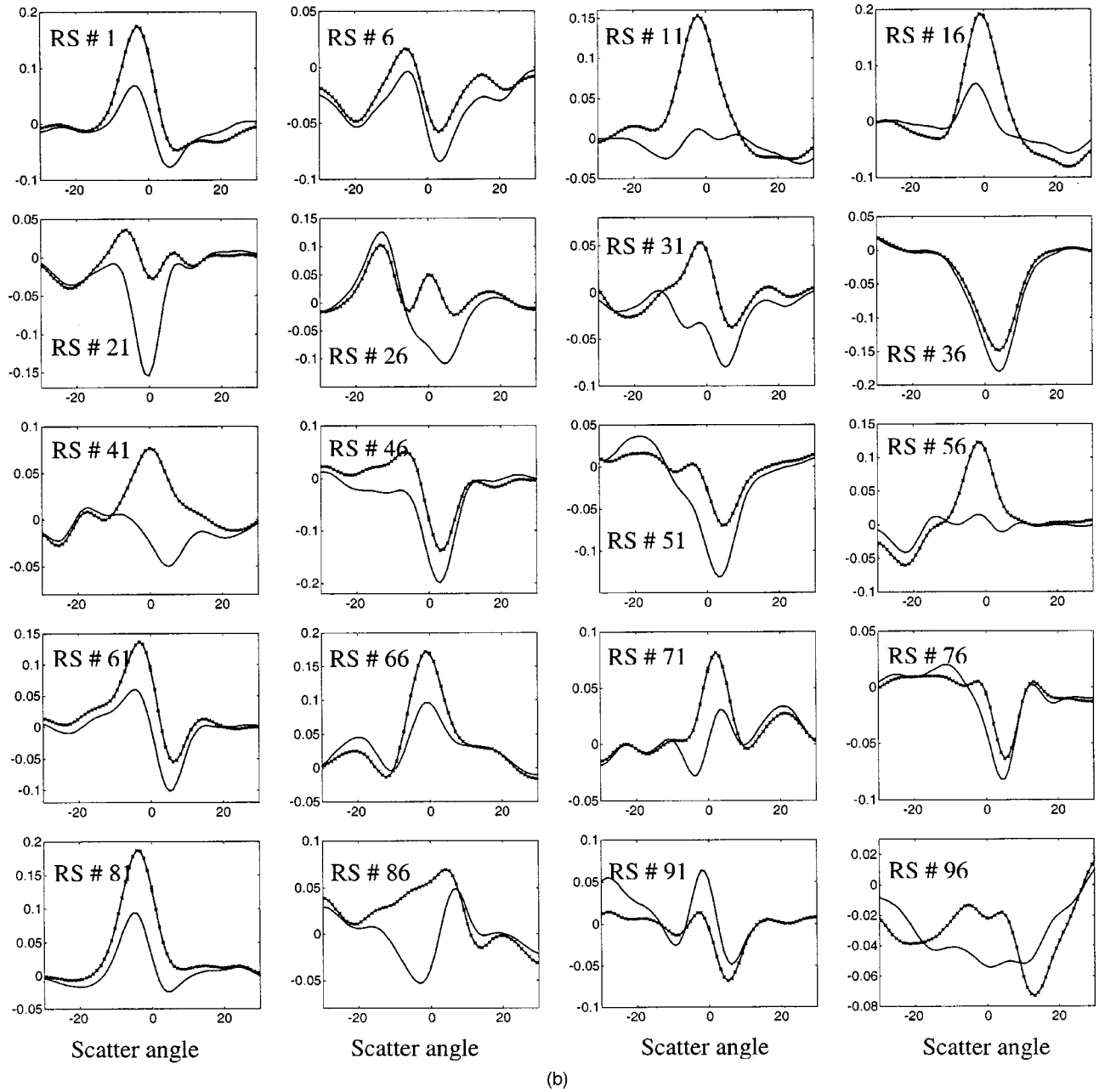

Fig. 9. Normalized bistatic modified Mueller matrix element for (a) m_{11} (vv), and (b) m_{41} versus scatter angle for 20 individual rough surface realizations chosen from the 100 samples. Solid curve, for the rough ground only; cross symbol, for the rough ground with the horizontal 30°-tilted buried cylinder of Fig. 1(c). The incident angles are $\theta^i = 0°$ and $\phi^i = 0°$. No averaging.

$$L_{1,2}\mathbf{X} = \int_{S_1}\left[i\omega\mu_{1,2}\Phi_{1,2}\mathbf{X}(\mathbf{r}') + \frac{i}{\omega\epsilon_{1,2}}\nabla\nabla' \cdot \mathbf{X}(\mathbf{r}')\Phi_{1,2}\right]ds',$$

$$K_{1,2}\mathbf{X} = \int_{S_1}\mathbf{X}(\mathbf{r}') \times \nabla\Phi_{1,2}ds', \tag{A1}$$

$$L_{3,5}\mathbf{X} = \int_{S_2}\left[i\omega\mu_{2,3}\Phi_{2,3}\mathbf{X}(\mathbf{r}') + \frac{i}{\omega\epsilon_{2,3}}\nabla\nabla' \cdot \mathbf{X}(\mathbf{r}')\Phi_{2,3}\right]ds',$$

$$K_{3,5}\mathbf{X} = \int_{S_2}\mathbf{X}(\mathbf{r}') \times \nabla\Phi_{2,3}ds', \tag{A2}$$

$$L_{4,6}\mathbf{X} = \int_{S_3}\left[i\omega\mu_{2,4}\Phi_{2,4}\mathbf{X}(\mathbf{r}') + \frac{i}{\omega\epsilon_{2,4}}\nabla\nabla' \cdot \mathbf{X}(\mathbf{r}')\Phi_{2,4}\right]ds',$$

$$K_{4,6}\mathbf{X} = \int_{S_3}\mathbf{X}(\mathbf{r}') \times \nabla\Phi_{2,4}ds'. \tag{A3}$$

APPENDIX B

The linear system of equations, $\mathcal{Z}\mathcal{I} = \mathcal{V}$, is given by[1,3,9]

$$\begin{bmatrix} \mathcal{Z}_{11} & \mathcal{Z}_{12} & \mathcal{Z}_{13} \\ \mathcal{Z}_{21} & \mathcal{Z}_{22} & \mathcal{Z}_{23} \\ \mathcal{Z}_{31} & \mathcal{Z}_{32} & \mathcal{Z}_{33} \end{bmatrix} \begin{pmatrix} I^1 \\ I^2 \\ I^3 \end{pmatrix} = \begin{pmatrix} \mathcal{V}_1 \\ 0 \\ 0 \end{pmatrix}, \tag{B1}$$

where the submatrix $\mathcal{Z}_{11}$ is

$$\mathcal{Z}_{11} = \begin{bmatrix} \langle \mathbf{j}_1, (L_1 + L_2)\,\mathbf{j}_1 \rangle_{S_1} & \langle \mathbf{j}_1, -\eta_1 (K_1 + K_2)\,\mathbf{j}_1 \rangle_{S_1} \\ \langle \mathbf{j}_1, \eta_1 (K_1 + K_2)\,\mathbf{j}_1 \rangle_{S_1} & \left\langle \mathbf{j}_1, \eta_1^2 \left(\frac{L_1}{\eta_1^2} + \frac{L_2}{\eta_2^2} \right) \mathbf{j}_1 \right\rangle_{S_1} \end{bmatrix}, \tag{B2}$$

in which $\langle \mathcal{A}, \mathcal{B} \rangle_S$ denotes the complex inner product between vector functions $\mathcal{A}$ and $\mathcal{B}$ on a surface S. The submatrices $\mathcal{Z}_{12}$, $\mathcal{Z}_{13}$, and $\mathcal{Z}_{23}$ are given by

$$\mathcal{Z}_{12} = \begin{bmatrix} \langle \mathbf{j}_1, -L_3\,\mathbf{j}_2 \rangle_{S_1} & \langle \mathbf{j}_1, \eta_1 K_3\,\mathbf{j}_2 \rangle_{S_1} \\ \langle \mathbf{j}_1, -\eta_1 K_3\,\mathbf{j}_2 \rangle_{S_1} & \left\langle \mathbf{j}_1, -\eta_1^2 \left(\frac{L_3}{\eta_2^2} \right) \mathbf{j}_2 \right\rangle_{S_1} \end{bmatrix},$$

$$\mathcal{Z}_{13} = \begin{bmatrix} \langle \mathbf{j}_1, -L_4\,\mathbf{j}_3 \rangle_{S_1} & \langle \mathbf{j}_1, \eta_1 K_4\,\mathbf{j}_3 \rangle_{S_1} \\ \langle \mathbf{j}_1, -\eta_1 K_4\,\mathbf{j}_3 \rangle_{S_1} & \left\langle \mathbf{j}_1, -\eta_1^2 \left(\frac{L_4}{\eta_2^2} \right) \mathbf{j}_3 \right\rangle_{S_1} \end{bmatrix}, \tag{B3}$$

$$\mathcal{Z}_{23} = \begin{bmatrix} \langle \mathbf{j}_2, L_4\,\mathbf{j}_3 \rangle_{S_2} & \langle \mathbf{j}_2, -\eta_1 K_4\,\mathbf{j}_3 \rangle_{S_2} \\ \langle \mathbf{j}_2, \eta_1 K_4\,\mathbf{j}_3 \rangle_{S_2} & \left\langle \mathbf{j}_2, \eta_1^2 \frac{L_4}{\eta_2^2} \mathbf{j}_3 \right\rangle_{S_2} \end{bmatrix}. \tag{B4}$$

Similar expressions can be obtained for all the other submatrices in Eq. (B1).

ACKNOWLEDGMENTS

This research was sponsored in part by Northeastern University's Demining Multi-University Research Initiative grant DAA 0-55-97-0013, Engineering Research Centers Program of the National Science Foundation award EEC-9986821, and Arkansas Science and Technology Authority grant AR/ASTA/01-B-18.

The author can be reached by e-mail at magda @uark.edu.

REFERENCES

1. M. El-Shenawee, C. Rappaport, E. Miller, and M. Silevitch, "Three-dimensional subsurface analysis of electromagnetic scattering from penetrable/PEC objects buried under rough surfaces: use of the steepest descent fast multipole method (SDFMM)," IEEE Trans. Geosci. Remote Sens. **39**, 1174–1182 (2001).
2. M. El-Shenawee, C. Rappaport, and M. Silevitch, "Monte Carlo simulations of electromagnetic wave scattering from a random rough surface with three-dimensional penetrable buried object: mine detection application using the steepest-descent fast multipole method," J. Opt. Soc. Am. A **18**, 3077–3084 (2001).
3. M. El-Shenawee, "Scattering from multiple objects buried under two-dimensional randomly rough surface using the steepest descent fast multipole method," IEEE Trans. Antennas Propag. (to be published).
4. G. Zhang, L. Tsang, and K. Pak, "Angular correlation function and scattering coefficient of electromagnetic waves scattered by a buried object under a two-dimensional rough surface," J. Opt. Soc. Am. A **15**, 2995–3002 (1998).
5. Y. Zhang and E. Bahar, "Mueller matrix elements that characterize scattering from coated random rough surfaces," IEEE Trans. Antennas Propag. **47**, 949–955 (1999).
6. A. Ishimaru, *Wave Propagation and Scattering in Random Media* (Academic, New York, 1978).
7. F. T. Ulaby and C. Elachi, *Radar Polarimetry for Geoscience Applications* (Artech House, Norwood, Mass., 1990).
8. G. G. Stokes, "On the composition and resolution of streams of polarized light from different sources," Trans. Cambridge Philos. Soc. **9**, 399–416 (1852). Reprinted in *Mathematical and Physical Papers* (Cambridge U. Press, London, 1901), Vol. 3, pp. 233–250.
9. L. Medgyesi-Mitschang, J. Putnam, and M. Gedera, "Generalized method of moments for three-dimensional penetrable scatterers," J. Opt. Soc. Am. A **11**, 1383–1398 (1994).
10. S. M. Rao, D. R. Wilton, and A. W. Glisson, "Electromagnetic scattering by surfaces of arbitrary shape," IEEE Trans. Antennas Propag. **AP-30**, 409–418 (1982).
11. V. Jandhyala, "Fast multilevel algorithms for the efficient electromagnetic analysis of quasi-planar structures," Ph.D. dissertation (University of Illinois at Urbana-Champaign, Urbana-Champaign, Ill. 1998.
12. C. A. Balanis, *Advanced Engineering Electromagnetics* (Wiley, New York, 1989).
13. P. Tran and A. A. Maradudin, "Scattering of a scalar beam from a two-dimensional randomly rough hard wall: enhanced backscatter," Phys. Rev. B **45**, 3936–3939 (1992).
14. R. L. Wagner, J. Song, and W. C. Chew, "Monte Carlo simulation of electromagnetic scattering from two-dimensional random rough surfaces," IEEE Trans. Antennas Propag. **45**, 235–245 (1997).